

Numerical Study of Noise Sources Generated by Wing of Supersonic Business Jet in Landing Mode

Tatiana K. Kozubskaya¹ , Gleb M. Plaksin¹ , Ivan L. Sofronov² , Pavel V. Rodionov¹ 

© The Authors 2025. This paper is published with open access at SuperFri.org

The paper is devoted to the numerical study of wing noise for the prototype of supersonic business jet in landing mode. Near the wing, the acoustics is simulated using the CFD/CAA methods within the Delayed Detached Eddy Simulation approach. The Ffowcs Williams–Hawkings method is used for calculation of noise radiation in the far field. To localize the near-field acoustic sources, the advanced postprocessing including the numerical beamforming method is applied. The numerical beamforming formulated for monopole- and dipole-type sources allowed for detecting the main sources of the wing noise in the vicinity of leading and trailing edges. Analysis of the sound pressure level calculated for signals recorded on the Ffowcs Williams–Hawkings surface during the CFD simulations generally confirmed these results. Direct comparison of the noise spectra calculated by the Ffowcs Williams–Hawkings and numerical beamforming methods is provided for selected mid-field points. According to the presented noise radiation pattern, the far-field noise generated by the considered wing in landing mode has dominating dipole-type component for frequencies lower than 250 Hz and dominating monopole-type component for frequencies higher than 1 kHz.

Keywords: supercomputer simulation, supersonic business jet, acoustic source, computational fluid dynamics, computational aeroacoustics, numerical beamforming, monopole, dipole, turbulent flow, unstructured mesh.

Introduction

The design of modern civil aircraft, even at the earliest stages, includes not only optimization of aerodynamic characteristics, but also the reduction of total aircraft noisiness. The main impetus to the noise reduction arises from the severe requirements of International Civil Aviation Organization (ICAO) regarding the level of noise generated by civil aircraft near airports. These requirements apply to all types of civil aircraft including supersonic business jets (SSBJ) which are currently being developed in different countries.

Nowadays, numerical simulation is an important design tool widely used in the aerospace industry. While numerical assessment of aerodynamic characteristics has already become a standard component of the design process, numerical assessment of acoustic characteristics for aerospace problems is still in the development and implementation phase due to its high computational cost. Fortunately, the constantly increasing performance and availability of modern supercomputer clusters make aeroacoustic simulations feasible for single high-priority evaluations. In this paper, we present the results of aeroacoustic simulation for prototype of SSBJ airframe in landing mode.

Numerical assessment of acoustic characteristics of an aircraft is primarily based on resource-intensive CFD (Computational Fluid Dynamics) simulations of unsteady turbulent flow. Such simulations, sometimes referred to as eddy-resolving or scale-resolving, require to resolve high-energy turbulent eddies on computational grid and allow modeling the smaller-scale turbulence from inertial range by subgrid models. Note that for reliable results of scale-resolving simulations the characteristic mesh size in the region of unsteady turbulent flow should belong to inertial

¹Keldysh Institute of Applied Mathematics, RAS, Moscow, Russian Federation

²Moscow Institute of Physics and Technology, Dolgoprudny, Moscow Region, Russian Federation

range of turbulence scales. For airframe noise simulations, there are two main approaches currently in use: the first is Detached Eddy Simulation (DES) [6, 7, 19, 25] based on hybridization of Reynolds averaged Navier–Stokes (RANS) method and Large Eddy Simulation (LES), and the second is the lattice Boltzmann method (LBM) [5, 8, 14, 15, 22]. In the present paper, we follow the DES approach to simulate the noise of turbulent flow over the SSBJ wing.

During scale-resolving CFD/CAA (Computational Aeroacoustics) simulations a huge amount of raw numerical data can be extracted from the obtained flow fields. However, to get practically useful information about the target flow, accumulated data should be properly processed by specialized methods and techniques. The great example of such postprocessing methods is the Ffowcs Williams–Hawkings (FWH) method [9] that allows to calculate acoustics at arbitrary far-field points by processing the near-field signals at special discretized surface. Another example of postprocessing methods is conventional beamforming [26, 30]. This method is widely used during wind-tunnel experiments and flight tests to localize and evaluate the noise sources generated by considered geometry or aircraft by processing signals recorded with far-field microphone arrays. In the recent papers [13, 16, 17, 21], we develop a novel method to localize and evaluate the near-field acoustic sources using CFD data – *the numerical beamforming* based on processing signals recorded with an arbitrarily large number of virtual near-field microphones moving with the considered object. One of the important features of our approach is that the formulation of the problem and the method of its solution do not require any a priori assumptions about whether the acoustic source is correlated or uncorrelated. In the present study, we apply the numerical beamforming to detect the noise sources generated by the SSBJ wing in landing mode. It is for the first time that this method is used to analyze acoustics of the full-scale aircraft geometry.

We should note that the numerical beamforming method solves the inverse problem regarding the near-field acoustic signals extracted from CFD simulation. Hence, the numerical beamforming has typical characteristics of inverse problems such as ill-posedness and solution non-uniqueness.

The paper consists of three sections. The first section is devoted to the scale-resolving simulations of turbulent flow near the prototype of SSBJ airframe in landing mode. This section presents the obtained characteristics of acoustic pressure pulsations near the leading and trailing edges of the SSBJ wing, at the far-field points and on the FWH surface. The second section formulates the numerical beamforming method for monopole-, dipole-type sources and describes the computational setup used to localize and evaluate the noise sources generated by the SSBJ wing. In the third section the results of numerical beamforming for the SSBJ wing in landing mode are discussed.

1. Scale-Resolving Simulations of Wing Noise

1.1. Problem Formulation

The full-scale airframe of SSBJ prototype [7] with $10^\circ - 10^\circ$ deflection of droop noses and $10^\circ - 20^\circ - 20^\circ - 10^\circ$ deflection of elevons on each side of the wing (Fig. 1) is placed inside the uniform airflow with the velocity $U_\infty = 68$ m/s, the pressure $P_\infty = 101325$ Pa and the temperature $T_\infty = 288.15$ K at an angle of attack 10° . The length of the considered geometry is 45 m, the wingspan is 20 m. The corresponding Mach number is 0.2, the Reynolds number based on the characteristic length $L = 1$ m is 4.6×10^6 .

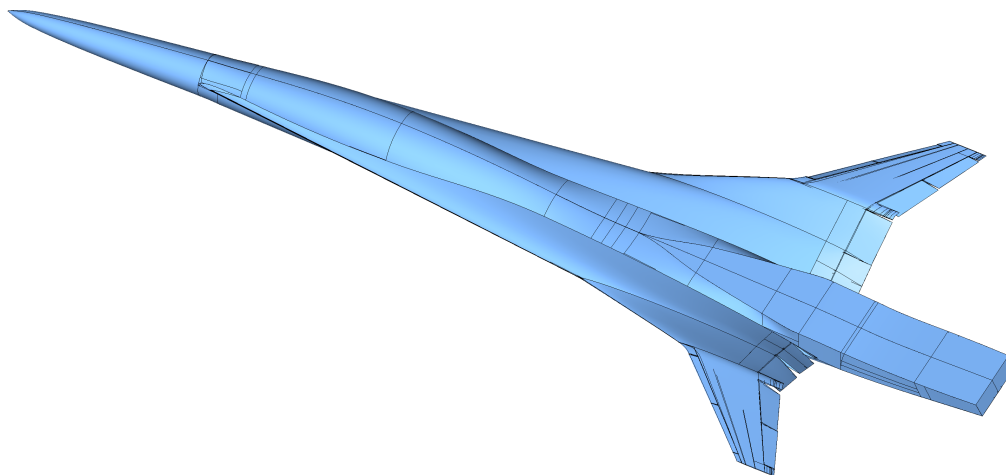


Figure 1. Airframe of SSBJ prototype with high-lift devices in landing configuration [7]

1.2. Computational Setup

To model noise of the SSBJ wing in near field, we perform scale-resolving simulations according to the Delayed Detached Eddy Simulation (DDES) approach [19, 25] with the subgrid scale $\Delta = \tilde{\Delta}_\omega$ [19] and the sigma subgrid-scale model [20] in the LES region and the Spalart–Allmaras (SA) turbulence model [27] in the RANS region. To model the properties of air, we use the calorically perfect gas with the ratio of specific heats $\gamma = 1.4$ and the specific gas constant $R_{\text{sp}} = 287.05 \text{ J}/(\text{kg K})$.

Due to the symmetry of the considered geometry and the problem parameters, we simulate the flow only for half of the airframe. This approach allows us to significantly reduce the computational costs of simulations. However, it eliminates asymmetric features of the flow that could potentially arise if the problem is solved in the entire region. All the acoustic data presented in the paper is calculated for half of the airframe as well. Because the acoustic sources located on different sides of the airframe are spatially separated, we can consider them as uncorrelated. Hence, to obtain sound intensity for the full airframe in far field, one can increase the corresponding intensity for half of the geometry by 3 dB.

The slip boundary conditions are set at the plane of symmetry $y = 0$, the free-stream conditions are used at the outer boundaries. Zero velocity and zero heat flux are specified on the streamlined geometry. To prevent the reflection of acoustic waves from the plane of symmetry in DDES simulations, the sponge layer [10] based on the averaged RANS solution is set in the region $0 \text{ m} \leq z \leq 1.5 \text{ m}$.

The computational domain is defined by the parallelepiped $2000 \text{ m} \times 2000 \text{ m} \times 1000 \text{ m}$ with the exclusion of SSBJ airframe interior. The center of the boundary at the plane of symmetry is located 31.5 m away from the SSBJ fore point along the x -axis.

We use the finite-volume vertex-centered EBR5 PL scheme [4] to approximate the convective flux and the method of local element splittings [3] to approximate the diffusive flux. For time integration, we apply the second-order implicit scheme based on the backward differentiation formula (BDF2). To solve the system of nonlinear equations at each time step, we use two Newton iterations. At each iteration, we solve the system of linear equations by the bi-conjugate gradient stabilized (BiCGStab) method [29] with the symmetric Gauss–Seidel (SGS) preconditioner.

Simulations are performed on two meshes denoted as Level A and Level B. Their general structure is shown in Fig. 2, their parameters are summarized in Tab. 1, where h_{fuselage} is the length of mesh edges in tangential directions near the fuselage and the lower surface of the wing, h_{vortices} is the length of mesh edges in the region of stable vortex flow over the wing. Outside the prismatic layers built near the streamlined geometry, the zone of increased mesh resolution over the wing is filled with an isotropic unstructured tetrahedral mesh.

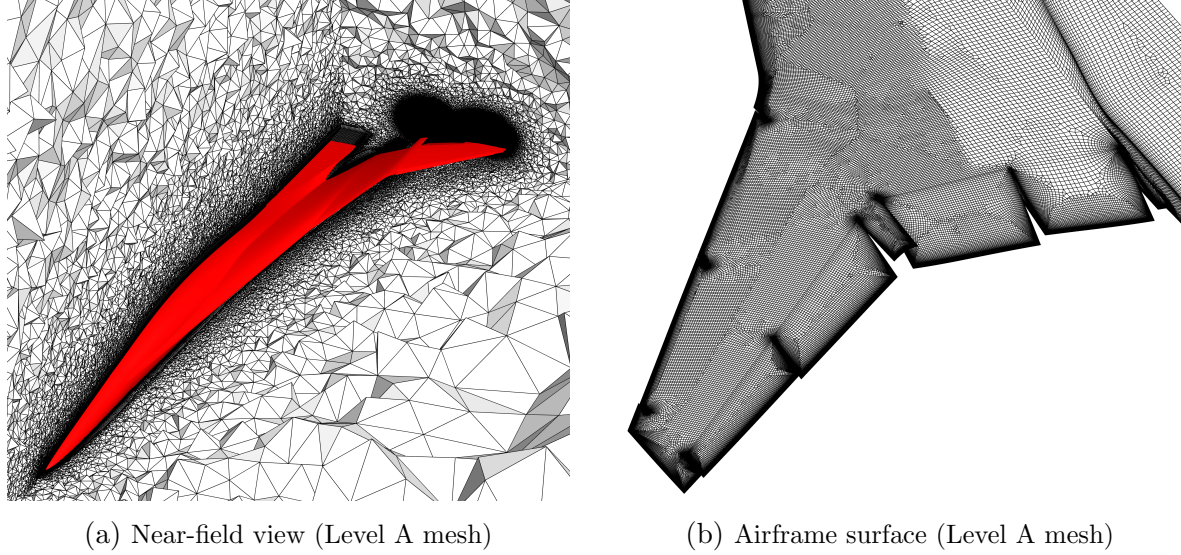


Figure 2. General mesh structure

Table 1. Mesh parameters

Mesh	N_{nodes}	N_{elements}	$N_{\text{surf.nodes}}$	$N_{\text{surf.elements}}$	h_{fuselage}	h_{vortices}
Level A	21 166 948	46 552 132	337 330	342 475	70 mm	35 mm
Level B	61 601 940	219 587 977	678 233	687 362	70 mm	17.5 mm

We decrease the weight of upwind component of the EBR5 PL scheme according to the approach proposed in [12]. The minimum weight of upwind component in the zone of increased mesh resolution over the wing is set to 0.15. We choose the values of time step that provide relatively small regions of numerical instability. In terms of $\text{CFL}_{\text{vortices}} = \Delta t \times (c_{\infty} + U_{\infty}) / h_{\text{vortices}}$, where Δt is the time step and c_{∞} is the speed of sound at infinity, we use $\text{CFL}_{\text{vortices}} = 0.083$ on the Level A mesh and $\text{CFL}_{\text{vortices}} = 0.125$ on the Level B mesh. When the flow is reached the steady state and the instantaneous solution is proved to have only small regions of numerical instability, we start to record the near-field acoustic data. The data recording is performed for time interval $60 L/U_{\infty}$ or 0.88 s. This interval size allows us to obtain smoothed spectra (averaged for 30 time segments with 0.5 overlapping) at the near-field and far-field points with the minimum resolved frequency 20 Hz.

All the DDES simulations presented in this paper are performed using the NOISEtte code [1] written in C++ and suitable for computations in CPU, GPU (OpenCL) and heterogeneous CPU+GPU modes with combined MPI+OpenMP parallelization. The parallel efficiency of the NOISEtte code and its performance on various supercomputers are presented in [11]. The aforementioned simulations are carried out using NVIDIA Tesla V100 GPUs on the Lomonosov-2

supercomputer [28] installed at Lomonosov Moscow State University. For the DDES simulation on the Level A mesh, 8 GPUs (4 compute nodes each equipped with 2 GPUs) are utilized for 21 hours to accumulate the required data on the time interval $60 L/U_\infty$. For the DDES simulation on the Level B mesh, 24 GPUs (12 compute nodes) are utilized for 24 hours to achieve the steady flow state after starting from the instantaneous DDES solution obtained on the Level A mesh and for 72 hours to accumulate the required data on the time interval $60 L/U_\infty$.

1.3. Far-Field Noise Calculation

We use the second-order FWH method [2, 9, 23, 24] to calculate acoustic pressure pulsations in the far field. The corresponding FWH surface used to accumulate the required acoustic data during DDES simulations is located near the boundaries of the zone of increased mesh resolution and contains five end caps (Fig. 3). Note that this surface has a slit on the fuselage side to prevent intersection with the wing surface. The far-field points used to calculate noise radiation pattern belong to the sphere of radius 150 m (Fig. 3).

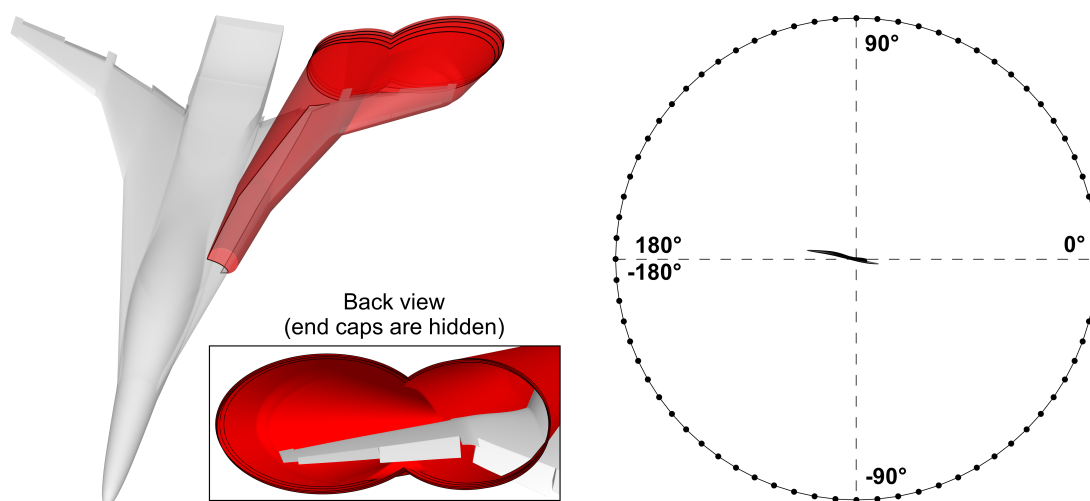


Figure 3. FWH surface and far-field points used to calculate noise radiation pattern

We accumulate the required acoustic data on the two types of meshes formed mainly by quadrilaterals. We use the label Coarse for isotropic meshes with edge length $2h_{\text{vortices}}$ and the label Fine for isotropic meshes with edge length h_{vortices} . We record the data with the sampling frequency $(c_\infty + U_\infty)/(2h_{\text{vortices}})$ on the Coarse FWH meshes and with the sampling frequency $(c_\infty + U_\infty)/h_{\text{vortices}}$ on the Fine FWH meshes.

The described methodology of far-field noise calculation has been tested for the SSBJ wing by comparing acoustic spectra obtained by direct DDES simulations and calculations based on the FWH method at some near-field points [7].

1.4. Numerical Results

In this section, we summarize the main results presented in [7] and supplement them with the new postprocessing data. For detailed information about DDES performance and flow aerodynamics of the SSBJ airframe in landing mode, see [7].

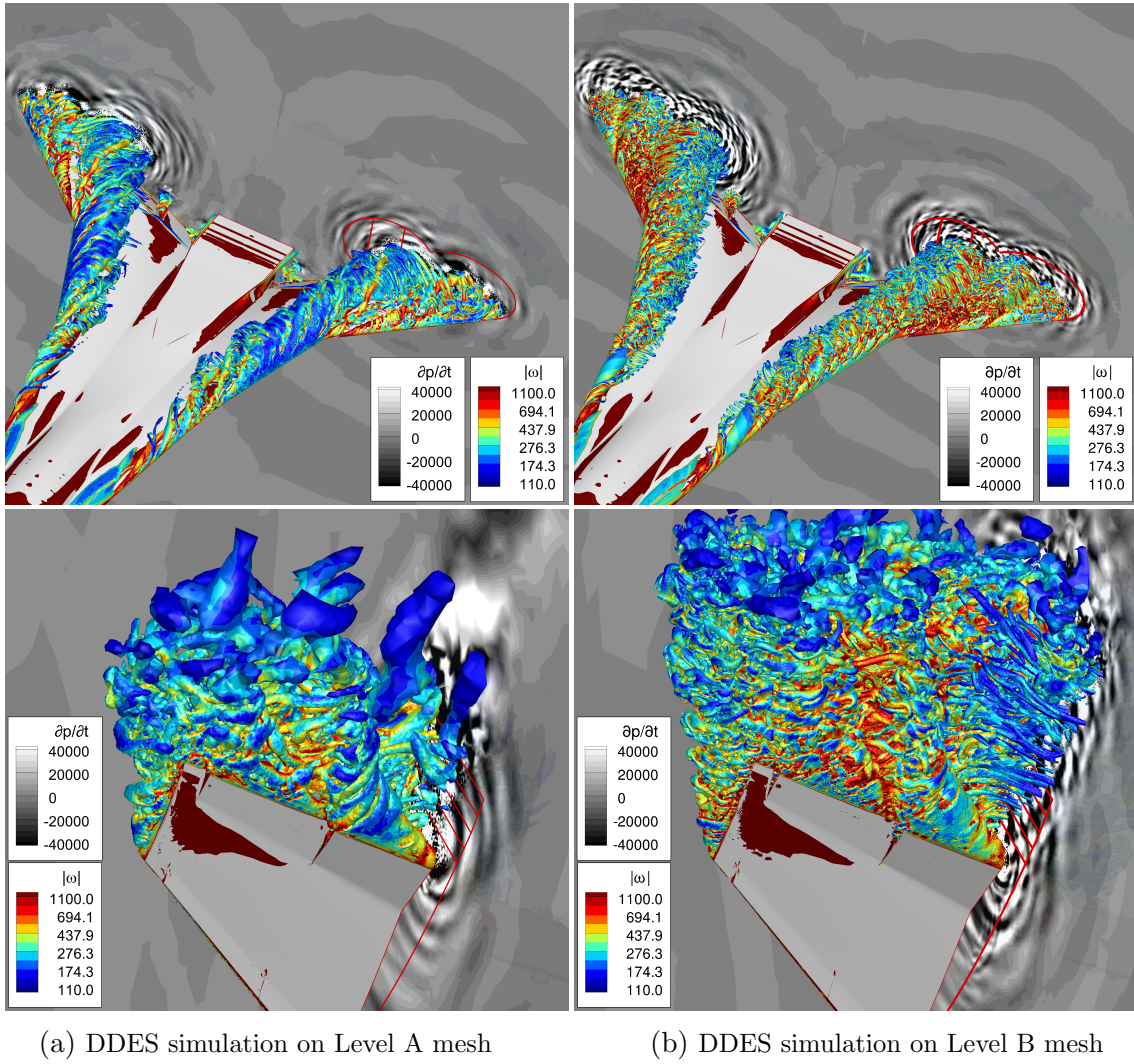
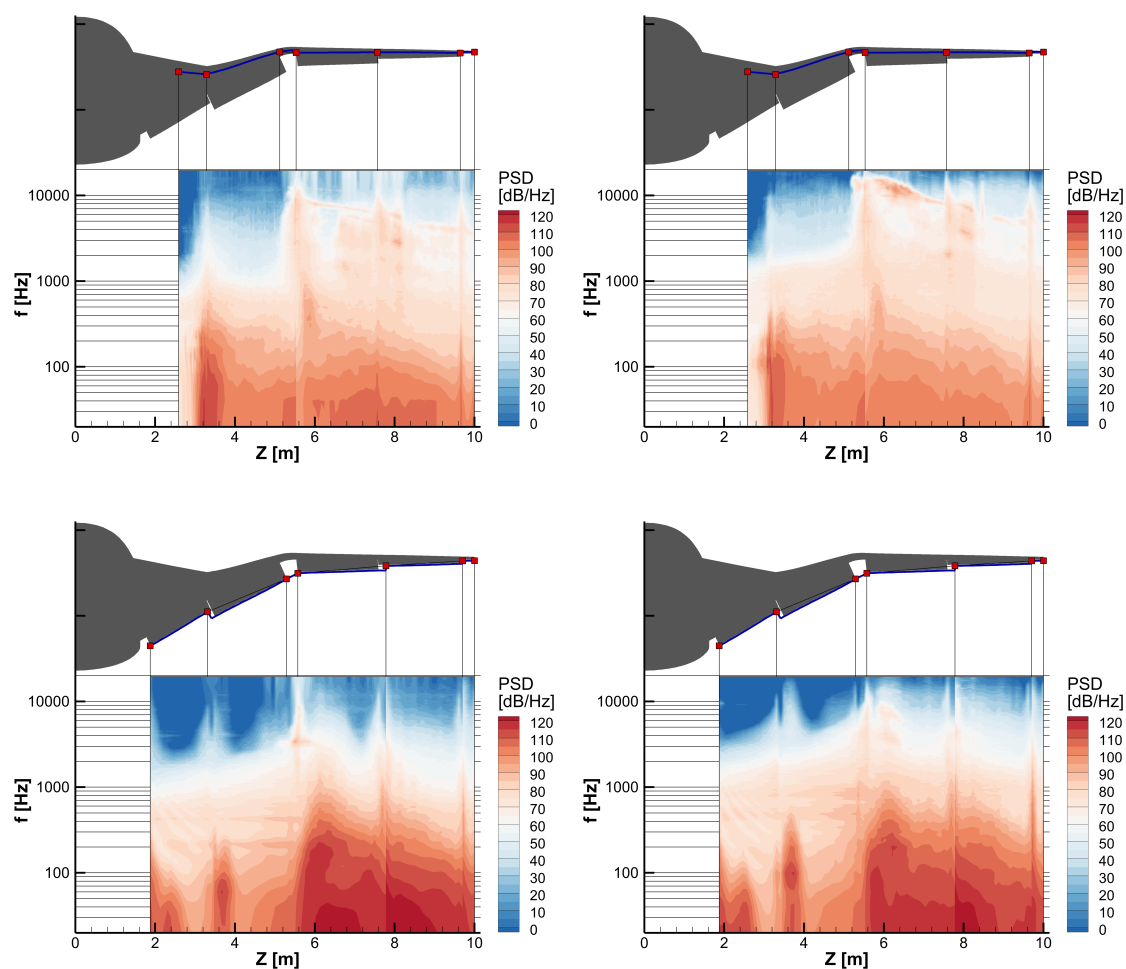


Figure 4. Instantaneous flow fields obtained by DDES simulations (time derivative of pressure and Q-criterion isosurfaces corresponding to the value 5000 1/s^2 colored by vorticity magnitude). The red curve denotes location of the FWH surface

The instantaneous flow fields obtained by DDES simulations after reaching the steady state are shown in Fig. 4. For visualization purposes, we duplicate and reflect the resulting flow fields relatively to the plane of symmetry $y = 0$. We see that the turbulent vortical flow over the wing is a source of acoustic pulsations. In the vicinity of the fuselage, the flow is almost stationary and does not contain any significant acoustic sources. As expected, the mesh refinement allows DDES method to reproduce smaller turbulent structures, which leads to the emergence of higher-frequency harmonics in the simulated noise. Outside the zone of increased mesh resolution over the wing acoustic pulsations rapidly dissipate due to increasing size of mesh edges.

During DDES simulations, we record pressure values with the sampling frequency $(c_\infty + U_\infty)/(h_{\text{vortices}}/4)$ at the points of the discretized curves located along the leading and trailing edges of the SSBJ wing. These curves are placed approximately 4 cm below the wing edge, the discretization step is approximately 10 cm. The corresponding power spectral density (PSD) of acoustic pressure pulsations is shown in Fig. 5. The presented spectra are broadband, and, at most points, the noise level decreases with increasing frequency. The similar features of

SSBJ wing noise are obtained in [15, 22]. Near the leading edge, we see the two main PSD peaks: the first is located near the point of sweep angle change at $z = 3.3$ m, the second is located at $z = 5.86$ m in a small distance from the fuselage-side tip of the first droop nose ($z = 5.53$ m). After comparing these results with the flow fields presented in Fig. 4, we can conclude that such PSD peaks are connected with the loss of vortex stability near the wing edge. This observation is confirmed by PSD plots for the trailing edge where the peak at $z = 6.13$ m is associated with the vortex over the third elevon that originates at the elevon fuselage-side tip ($z = 5.57$ m), the peaks at $z = 1.9$ m and $z = 2.5$ m are caused by the tip vortex and wing-root vortex over the first elevon, the peak at $z = 3.68$ m is caused by the tip vortex over the second elevon, the peak at $z = 7.75$ m is associated with the interaction of the stable vortex over the third elevon with the tip of the fourth elevon supplemented by tip vortex effects, and the peak at $z = 9.7$ m is associated with the complex vortex flow in a vicinity of the slit between the fourth elevon and the wing.



(a) DDES simulation on Level A mesh

(b) DDES simulation on Level B mesh

Figure 5. Power spectral density of acoustic pressure pulsations near the leading and trailing edges

Sound pressure level (SPL) for selected one-third octave bands at the centers of FWH mesh elements is shown in Fig. 6. The main intention of building such plots as well as the plots

presented in Fig. 5 is to demonstrate the possible types of acoustic data that can be directly extracted from DDES solution without involving more complex postprocessing methods such as beamforming or dynamic mode decomposition (DMD). Because valid acoustic spectrum can not be calculated for signal recorded at non-linear flow region, in Fig. 6 one should ignore the presented data at the parts of the FWH surface through which non-linear structures pass. Such parts are located at the side closest to the fuselage and near the end caps (see the corresponding irregular 105–110 dB SPL peaks at 250 Hz band obtained in the DDES simulation on the Level B mesh). The footprint of the acoustic sources near the point of sweep angle change is clearly visible at 250 Hz and 500 Hz bands. The approximate position of the noise sources associated with the vortex originating at the fuselage-side tip of the first droop nose can be seen at all demonstrated frequency bands. The footprints of the acoustic sources associated with the stable vortices over the elevons are localized along the trailing edge.

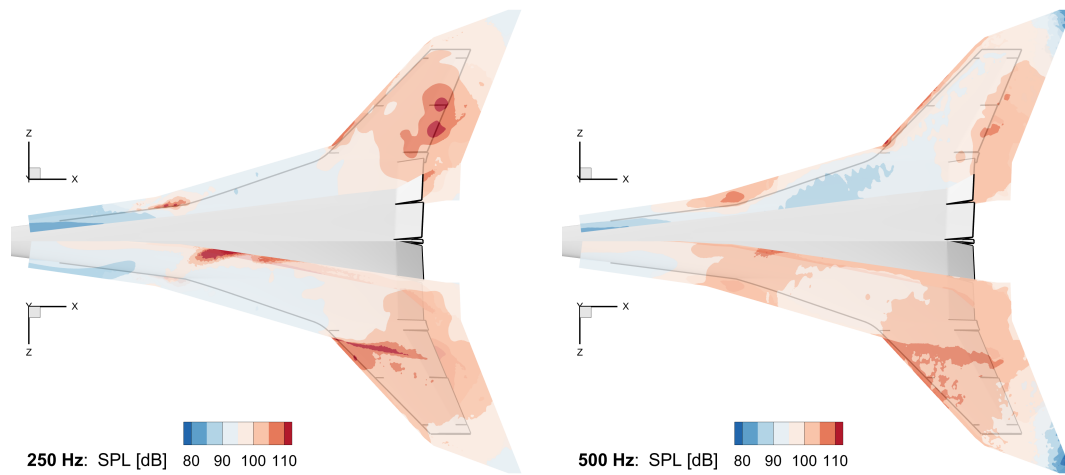
We should note that the noise level at FWH surface is highly dependent on its position and shape. Since we construct the FWH surface according to the approximate shapes of the stable vortices formed over the wing, this surface follows the shape of leading edge, but not the shape of trailing edge (see Fig. 3). Hence, the results presented in Fig. 5 and Fig. 6 are in good agreement for the leading edge, while for the trailing edge the results given in Fig. 5 are more reliable and correct.

Noise radiation pattern for selected one-third octave bands at the far-field points (Fig. 3) is demonstrated in Fig. 7. As expected, resulting radiation pattern depends on meshes used for DDES simulation and FWH calculation. We see that the replacement of Coarse FWH mesh with Fine FWH mesh leads to 2–3 dB SPL difference at 250–500 Hz bands for the data recorded on the Level A mesh and to 1–1.5 dB SPL difference at 250–2000 Hz bands for the data recorded on the Level B mesh. The SPL difference between the results obtained for the Level A and Level B meshes using Fine FWH mesh is 2–3.5 dB at 250 Hz band and 1.5–4 dB at 500 Hz band. At 250 Hz band noise radiation pattern for all DDES and FWH meshes has the dominating dipole-type component, which leads to local SPL maximums approximately at -100° and 80° and to local SPL minimums approximately at -10° and 170° . For the Level A mesh at 0.5–1 kHz bands and for the Level B mesh at 1–2 kHz bands, the obtained radiation patterns have the dominating monopole-type component, which provides SPL maximum between 100° and 160° and SPL minimum between -140° and -50° . For the Level B mesh, the noise radiation pattern at 500 Hz band probably has a mixed structure formed by both monopole-type and dipole-type components.

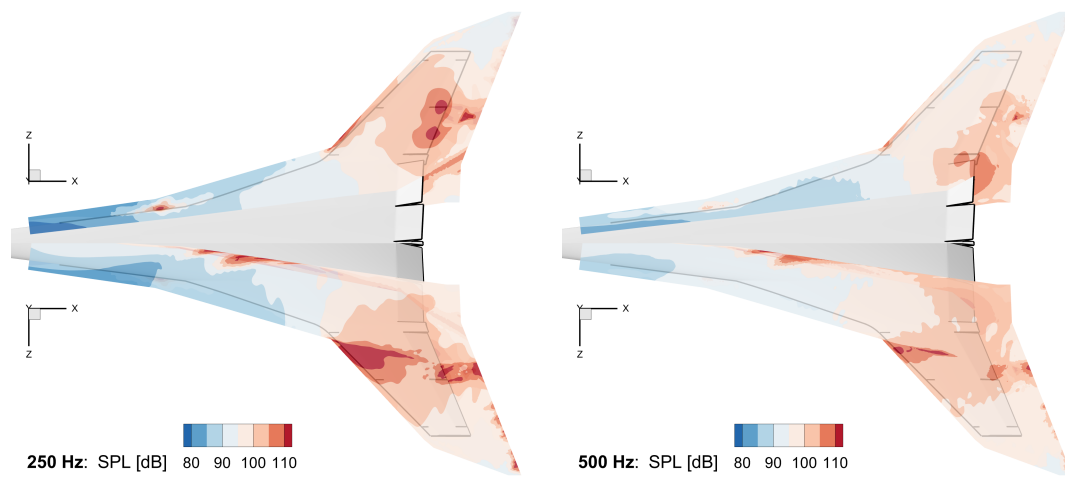
2. Inverse Problem – Numerical Beamforming

2.1. Problem Setup and Geometry

The aim of numerical beamforming is to identify acoustic sources in a certain regions (on a surface or on a line) using space-time data obtained by numerical simulation. For the considered method, the acoustic pressure pulsations recorded at some points of the computational domain are used as input data. Such points can be considered as virtual microphones, so we will refer to them as microphones in this paper. Microphones can be placed on surfaces, lines or in any other arbitrary way, in accordance with the selected source domain. The number of microphones can be chosen arbitrarily. As microphone surface used to identify acoustic sources on the wing of the SSBJ model, one can choose either the FWH surface (Fig. 3), or, in general, an arbitrary set of



(a) DDES simulation on Level A mesh (Fine FWH mesh)



(b) DDES simulation on Level B mesh (Coarse FWH mesh)

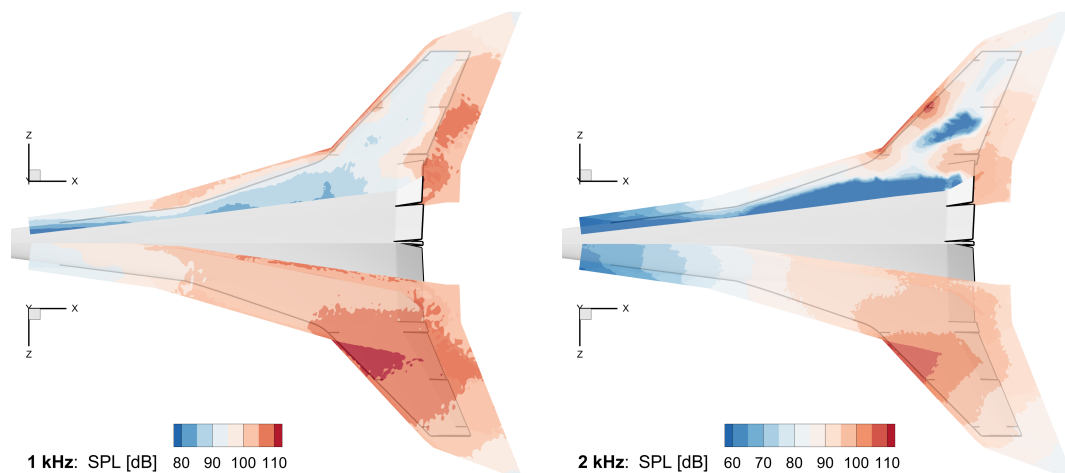


Figure 6. Sound pressure level at FWH surface for one-third octave bands with central frequencies 250 Hz, 500 Hz, 1 kHz and 2 kHz

points in the far field, at which the signal can be calculated using integral formulas according to the Ffowcs Williams–Hawkings acoustic analogy [9].

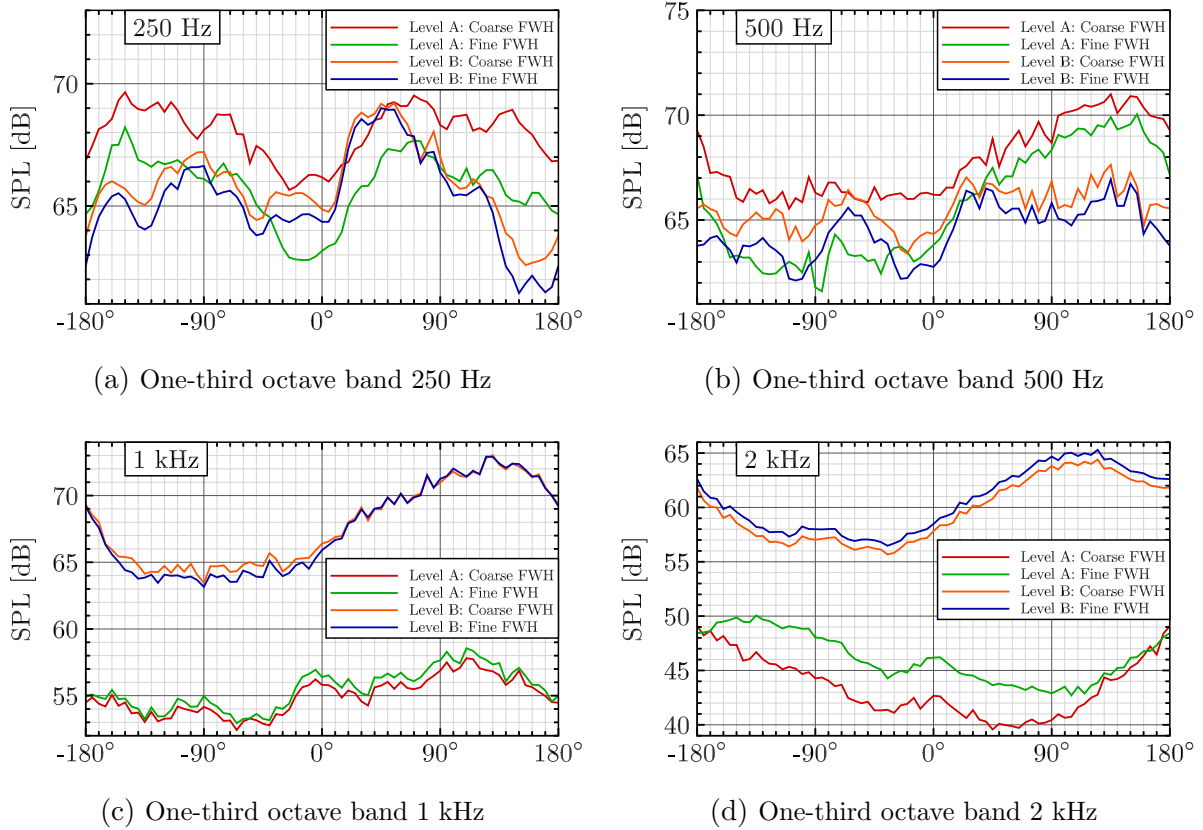


Figure 7. Noise radiation pattern ($R = 150$ m) for one-third octave bands with central frequencies 250 Hz, 500 Hz, 1 kHz and 2 kHz

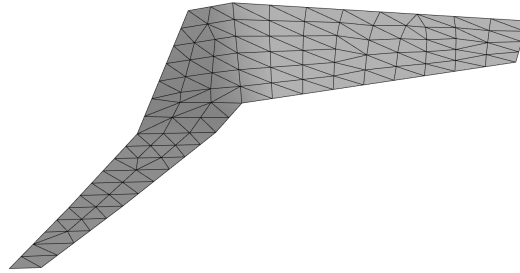
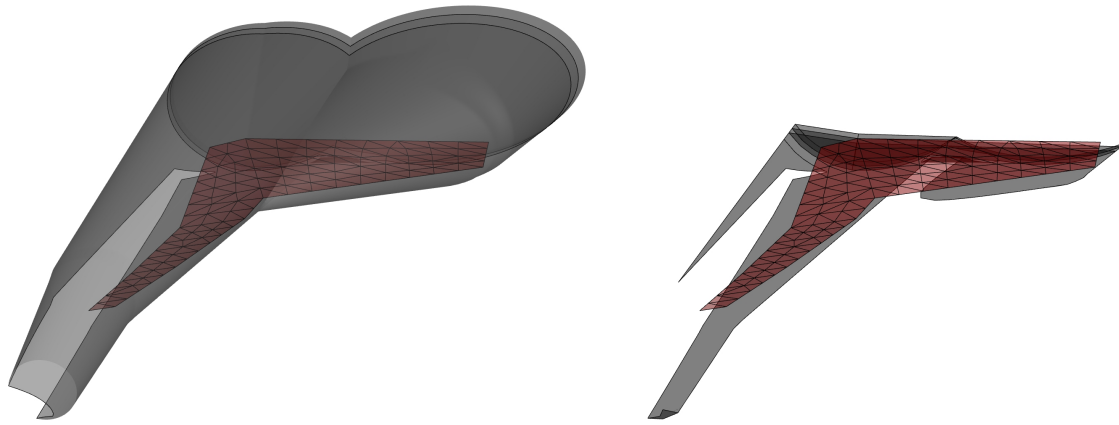


Figure 8. Example of a source grid for identifying an acoustic source on the SSBJ wing

The source domain is defined as a surface, in some sense approximating the wing of the SSBJ model (Fig. 8). As in [21], we consider two microphone configurations: one consists of points located on entire FWH surface (Fig. 9a) and another consists of points located on its lower part only (Fig. 9b). Microphones of the latter configuration record acoustics radiated toward the ground. This configuration is of practical interest and is sufficient for reliable reconstruction of the monopole source function. Nevertheless, there are configurations or types of acoustic sources which require the use of the entire FWH surface as microphone domain in order to ensure the solution uniqueness (see [21]). Thus, the aim of numerical beamforming for the SSBJ wing is to

localize and determine the intensity of the acoustic sources on the surface that approximates this wing using the acoustic signals recorded by microphones located in the spatial configurations described above.



(a) Entire FWH configuration

(b) Lower FWH configuration

Figure 9. Configurations of the source and microphone surfaces for the SSBJ wing

2.2. Numerical Method

The problem of acoustic beamforming for identifying a source on a given surface $S \subset \mathbb{R}^3$ defined by the delta function δ_S is formulated as the inverse problem of finding the right-hand side of the Helmholtz equation for the acoustic pressure $P(x)$ in a medium moving with a velocity U :

$$-\frac{1}{c^2}(i\omega + U \cdot \nabla)^2 P + \Delta P = -Q\delta_S - \text{div}(\mathbf{F}\delta_S), \quad (1)$$

where $Q(x) \in \mathbb{C}$, $x = \{x_1, x_2, x_3\} \in S$ is the unknown intensity of a monopole-type source, $F_l(x) \in \mathbb{C}$, $l = 1, 2, 3$ is the unknown intensity of a dipole moment in the direction of the Cartesian coordinate x_l , $\mathbf{F} \equiv \{F_1, F_2, F_3\}$, ω is the circular frequency, $c > U$ is the sound speed. To solve this problem, the values of acoustic pressure $P(x)$, $x \in D$, where D is some given microphone surface, are used, which are called *beamforming data* and are accumulated within the CFD/CAA simulation. A possible configuration of the source and microphone surfaces is shown in Fig. 10.

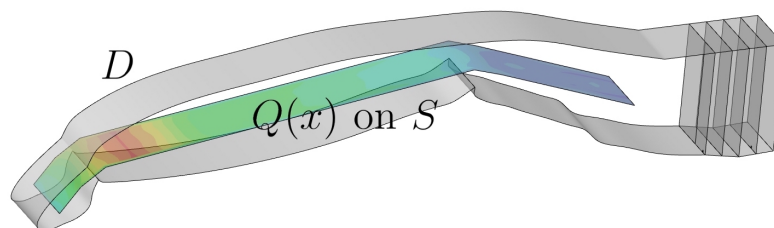


Figure 10. Configuration of the source (S) and microphone (D) surfaces

Monopole-type sources. The dependence of acoustic pressure in Eq. (1) on a monopole-type source given by the function Q is calculated using the surface potential

$$P(x) = \int_S Q(y) G_{\mathbf{M}}(x-y) d\sigma, \quad x \in D,$$

$$\text{where } G_{\mathbf{M}}(x) = \frac{1}{4\pi} \frac{e^{-ik' \Delta t_e}}{x'},$$

$$x' = \sqrt{(\mathbf{M} \cdot \mathbf{r})^2 + \beta^2 |\mathbf{r}|^2}, \quad \beta^2 = 1 - |\mathbf{M}|^2, \quad k' = \frac{\omega}{c\beta^2},$$

$$\Delta t_e = -(\mathbf{M} \cdot \mathbf{r}) + x'.$$

or in operator form:

$$P = \mathcal{T}Q.$$

The grids consisting of N and M nodes, respectively, are introduced on the surfaces of the source and microphones to construct a numerical method for solving the beamforming problem, $M \gg N$. The intensity function of a distributed monopole-type source is represented by its values s_n in the grid nodes in the form of a vector $\mathbf{s} = (s_1, s_2, \dots, s_N)^\top$ using the piecewise linear basis functions $\{\psi_n(y)\}_{n=1}^N$:

$$Q(y) = \sum_{n=1}^N s_n \psi_n(y),$$

while the pressure P at the microphone points is written in the form of a vector $\mathbf{d} = (d_1, d_2, \dots, d_M)^\top$. Thus, the radiation from the source to the microphones is transferred according to

$$\mathbf{d} = \mathcal{T}_a \mathbf{s} \tag{2}$$

where \mathcal{T}_a is a discrete approximation of the operator \mathcal{T} , which is obtained according to the finite element approach:

$$(\mathcal{T}_a)_{mn} = \int_S \psi_n(y) G_{\mathbf{M}}(x_m - y) d\sigma, \tag{3}$$

using Gauss formulas to calculate the integrals.

Given the *beamforming data* $\tilde{\mathbf{d}}$ at the microphone grid points the condition of minimizing the residual norm $\tilde{\mathbf{d}} - \mathbf{d}$ is set with the possible addition of Tikhonov regularization, $\gamma \geq 0$, to find the source intensity vector \mathbf{s} :

$$\|\tilde{\mathbf{d}} - \mathcal{T}_a \mathbf{s}\|_2^2 + \gamma \|\mathbf{s}\|_2^2 \rightarrow \min_{\mathbf{s}}.$$

The solution to such a problem has the form:

$$\mathbf{s} = (\mathcal{T}_a^* \mathcal{T}_a + \gamma I)^{-1} \mathcal{T}_a^* \tilde{\mathbf{d}}.$$

Analysis [16] shows that the numerical beamforming algorithm for monopole-type sources has high accuracy and good stability without using regularization if the following conditions are met:

$$\begin{aligned} M &\gg N \\ \text{dist}_S &= a_S \lambda, & 0.8 < a_S < 1.5 \\ \text{dist}_{SD} &= a_{SD} \lambda, & 3 < a_{SD} < 30, \end{aligned} \tag{4}$$

where dist_S is the source function grid step, dist_{SD} is the distance between surfaces S and D , $\lambda = 2\pi/k'$.

Dipole-type sources. For discretization of the problem in case of a dipole-type source, the same approach is used as for monopole-type sources. In this case, the radiation transfer matrix \mathcal{T}_a is formed from three component matrices \mathcal{T}_a^1 , \mathcal{T}_a^2 , \mathcal{T}_a^3 :

$$(\mathcal{T}_a^l)_{mn} = \int_S \psi_n(y) G_{\mathbf{M}}^{(l)}(x_m - y) d\sigma, \quad l = 1, 2, 3, \quad (5)$$

with the fundamental solutions $G_{\mathbf{M}}^{(l)}(x) = \frac{\partial}{\partial x_l} G_{\mathbf{M}}(x)$.

However, for dipole-type sources in the right-hand side of Eq. (1) the non-uniqueness of beamforming problem solution arises due to the presence of the surface divergence operator Div that vanishes any function of the form $\text{Curl}(\mathbf{a})$, where Curl is the surface curl operator. In [17] some restrictions on the dipole-type source are considered in order to address the non-uniqueness. For example, in case of a priori information that some dipole component is zero, it is excluded. Another useful restriction arises when the direction of the dipole moment, the unit vector $e(y)$, is known in advance at each grid node of the source,

$$e(y_n) = \{ \cos(\theta_n) \sin(\varphi_n), \cos(\theta_n) \cos(\varphi_n), \sin(\theta_n) \}, \quad n = 1..N, \quad (6)$$

(for example, $e(y)$ is the normal to the surface). In this case the resulting dipole radiation transfer matrix has the form:

$$\mathcal{T}_a^e = \mathcal{T}_a^1 \text{diag}(\cos \boldsymbol{\theta} \cdot \sin \boldsymbol{\varphi}) + \mathcal{T}_a^2 \text{diag}(\cos \boldsymbol{\theta} \cdot \cos \boldsymbol{\varphi}) + \mathcal{T}_a^3 \text{diag}(\sin \boldsymbol{\theta}).$$

Here $\cos \boldsymbol{\theta} = (\cos \theta_1, \cos \theta_2, \dots, \cos \theta_N)^\top$, $\sin \boldsymbol{\theta} = (\sin \theta_1, \sin \theta_2, \dots, \sin \theta_N)^\top$, $\cos \boldsymbol{\varphi} = (\cos \varphi_1, \cos \varphi_2, \dots, \cos \varphi_N)^\top$, $\sin \boldsymbol{\varphi} = (\sin \varphi_1, \sin \varphi_2, \dots, \sin \varphi_N)^\top$, and the lower dot symbol denotes component-wise multiplication of vectors: $\mathbf{a} \cdot \mathbf{b} \equiv (a_n b_n)_{n=1}^N$.

Note that from Eq. (1) follows the equivalence of considering the problems of finding both the monopole-type source $Q\delta_S$ and the tangential component $\text{Div}(\mathbf{F})\delta_S$ of the dipole-type source. Therefore, the question of the distribution of the found total intensity between these two types of sources can be solved only using a priori information.

2.3. Parallel Algorithms

The main resource-intensive part of the numerical beamforming algorithm is the calculation of the radiation transfer matrix. Even for relatively small number of nodes of source grid, which is limited on a source surface with fixed area by the condition Eq. (4) and which cannot be increased sufficiently to study the convergence of the method, it is necessary to calculate integral convolutions of piecewise linear basis functions with fundamental solutions of the Helmholtz equation for a moving medium (see Eq. (3), (5)). These integrals are calculated using Gauss formulas in double-precision complex numbers.

In order to speed up the numerical beamforming algorithm, the code implements MPI+OpenMP parallelization of the calculation of the radiation transfer matrix. Parallelization is performed along the matrix rows, since the number of microphones greatly exceeds the number of source grid nodes (each row corresponds to a single microphone, each column corresponds to a single node of source grid). Each process or thread is processing its own block of rows followed by data exchange in case of MPI parallelization. The dependence of speedup on the number of threads for OpenMP mode is showed in Fig. 11.

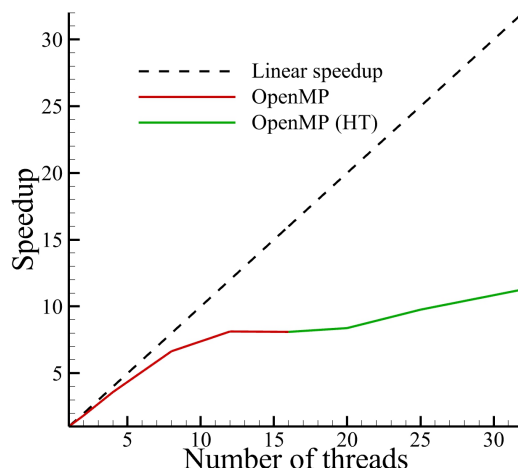


Figure 11. Dependence of speedup on the number of threads for OpenMP mode. The green line shows the speedup when using hyper-threading (HT)

Matrix calculation is also implemented for GPU using OpenCL framework. In GPU version of the algorithm, parallelization is implemented not only for rows, but also for columns. Heterogeneous computations show a significant speedup of the algorithm in comparison with the CPU version. The achieved speedup is mainly helpful for mass beamforming when a large number of frequency bands should be processed.

Even though we currently consider beamforming problems characterized by small dimensions of the radiation transfer matrix, the potential profit of parallel computations is rather high, especially for the industrial problems. In case of a fixed wavelength-matched grid step while the area of the surface can be of any size, the method has no upper limit on the number of microphones or source grid nodes.

2.4. Data Preprocessing

Beamforming based on CFD data processes pressure signals recorded at large number of points located in the region of linear perturbations. The most convenient approach is to use the points on the FWH surface. In many aeroacoustic simulations, the FWH surface is already used to accumulate near-field data required to calculate far-field noise. Hence, it is rather simple to add new variable, namely the pressure, in the list of variables to be recorded. On the other hand, different spatial microphone configurations may be required to refine resolution of acoustic sources obtained by beamforming (see [13]). Using the FWH method, one can easily calculate signals at the points of required microphone grids. In the present paper, microphone grid is located on the FWH surface only.

The signals extracted from CFD simulation usually contain spurious noise. To improve stability of the results obtained by the numerical beamforming method, it is useful to perform signal preprocessing with statistical averaging. Let us describe this algorithm in more detail. In the time domain, the starting point of the signal is randomly selected, and each starting point defines its own *scenario*. In this paper, we use 100 scenarios for signal preprocessing. For each scenario the signal is cut out and divided into several parts of equal length. These parts are averaged, the Fourier transformation is applied to the resulting signal, and the obtained data

corresponding to selected frequency band are used as input for the beamforming algorithm. This “stacking” approach allows to reduce the impact of spurious noise and leads to more stable results of numerical beamforming for neighboring frequency bands.

3. Numerical Beamforming for SSBJ Wing in Landing Mode

First, we apply the numerical beamforming to identify acoustic monopole-type sources on the wing of the SSBJ prototype using a microphone array located on the bottom of the FWH surface. This configuration of microphone grid is also used in [21] and allows to obtain a stable solution while capturing only the noise radiating towards the ground. Figure 12a presents the intensity map for the distributed monopole-type source obtained by numerical beamforming for the one-third octave band with central frequency $f_c = 500$ Hz. For each isolated point of distributed acoustic source, we calculate SPL at distance $\frac{1}{\sqrt{4\pi}}$ m according to [18]. Despite the high relative residual $\delta = 0.89$, the obtained solution for the monopole-type source is consistent with the results of the near-field analysis carried out in Section 1.4. As we see, the main noise sources are located near the wing edges, and the most intense ones are detected at the trailing edge.

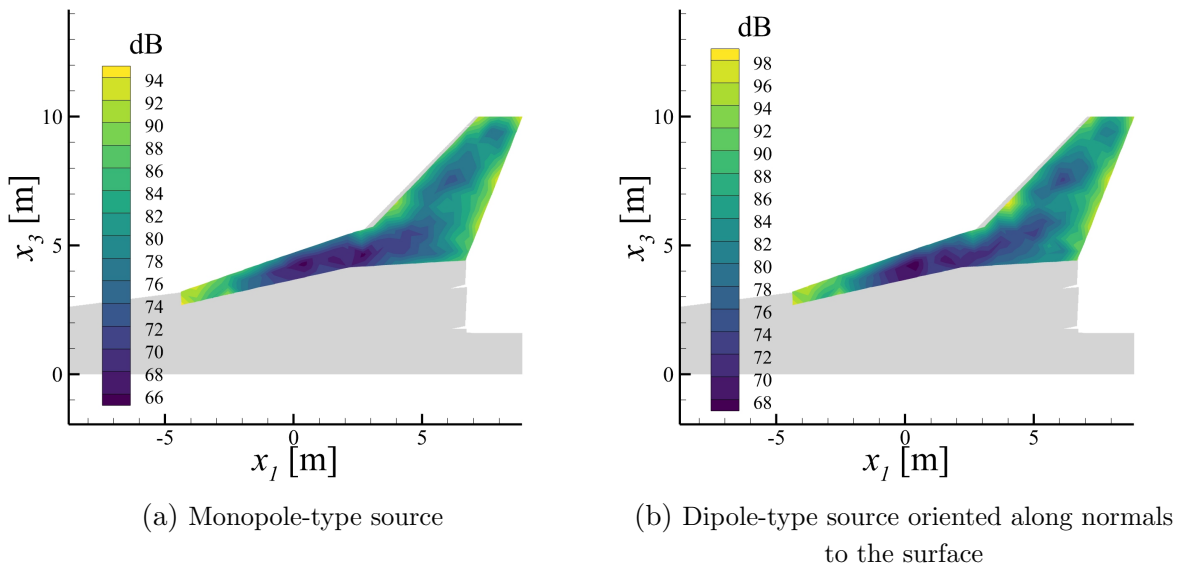


Figure 12. Numerical beamforming for the SSBJ wing and the one-third octave band with central frequency $f_c = 500$ Hz

For dipole-type sources oriented along normals to the surface, the numerical beamforming method demonstrates similar results (Fig. 12b). The microphone grid for detecting dipole-type sources coincides with the the microphone grid used for the monopole-type sources. The norm of relative residual is $\delta = 0.92$.

To assess the accuracy and reliability of the numerical beamforming, we compare SPL for the signals obtained at some mid-field points by the FWH method (the direct method) with SPL for the signals obtained at these points by the linear transfer of acoustic radiation from distributed sources reconstructed by the numerical beamforming (the inverse method). We use the following four points: $P_1 = (6, -10, 8)$, $P_2 = (7, -10, 8)$, $P_3 = (6, -10, 6)$, $P_4 = (7, -14, 8)$ (Fig. 13).

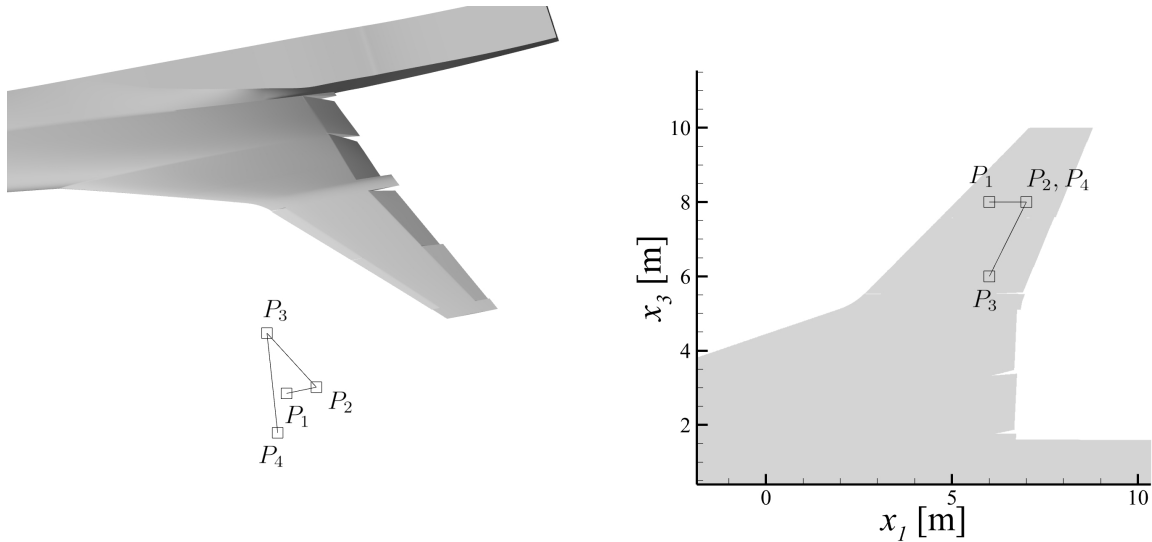


Figure 13. Location of points used to compare spectra obtained by FWH method and radiation transfer from the noise sources detected by numerical beamforming

To obtain the characteristics of pressure pulsations generated by detected acoustic sources, we perform mass beamforming by scanning over 1/12-octave bands for the frequency range $100 \text{ Hz} < f < 1000 \text{ Hz}$. For each 1/12-octave band, we use source grid of the required resolution that meets the *correctness* conditions (Eq. (4)) depending on the wavelength of the signal, and calculate the average source function. Then we compute signals at the points P_1 , P_2 , P_3 , P_4 using the obtained averaged source functions, according to Eq. (2). Finally, we calculate 1/12-octave band SPL spectra and convert them to 1/3-octave band SPL spectra by averaging and integration procedures.

In Fig. 14 and Fig. 15, the comparison of the SPL spectra for one-third octave bands at points P_1 , P_2 , P_3 and P_4 obtained by the FWH method and by radiation transfer from the noise sources detected by the numerical beamforming are presented. The green line corresponds to the results obtained by beamforming, and the dark gray one corresponds to direct calculations using the FWH method. The spectra obtained for the monopole-type source (Fig. 14) are in better agreement with the corresponding spectra based on FWH calculations (particularly, for point P_4) than the spectra obtained for the dipole-type source oriented along normals to the surface (Fig. 15). It is possible that the assumed source model in the form of the dipole, oriented along normals to the wing surface, can describe the real source localized on the wing worse due to the incorrectness of the assumption itself. We should note that the results for the monopole-type source can be interpreted as results for a dipole-type source with moment oriented tangentially to the surface (see Section 2.2). The dipole sources of this type are generated, for example, by a turbulent boundary layer.

Since the FWH and numerical beamforming methods are based on significantly different mathematical approaches, we do not expect the results obtained by these methods to coincide with each other with high accuracy. Despite the fact that the initial data for both methods are results of CFD computations accumulated on the same surface, when obtaining the values of acoustic pressure at the control points, the FWH method starts directly from these data, while numerical beamforming by its definition has its own model simplifications and assumptions. If we accept the above remark, we can speak about a very satisfactory reproduction of the results of the direct problem by beamforming.

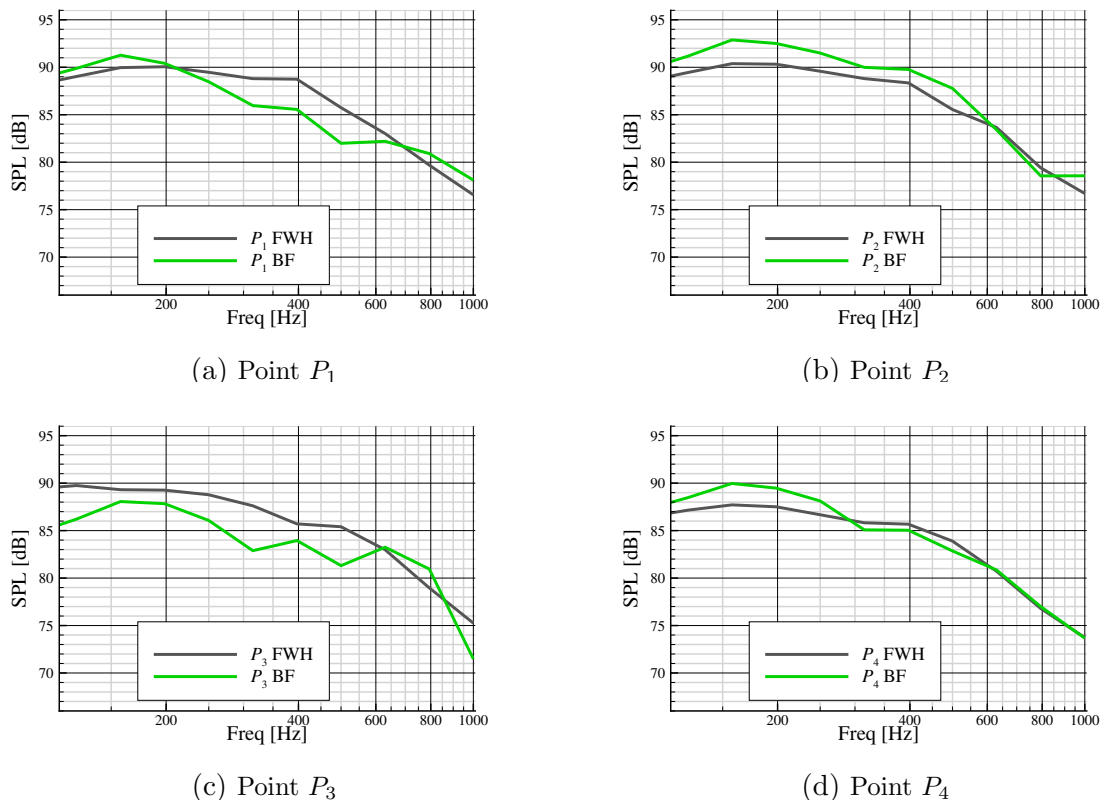


Figure 14. SPL spectra at mid-field points obtained by FWH and numerical beamforming (BF) methods. Monopole-type source

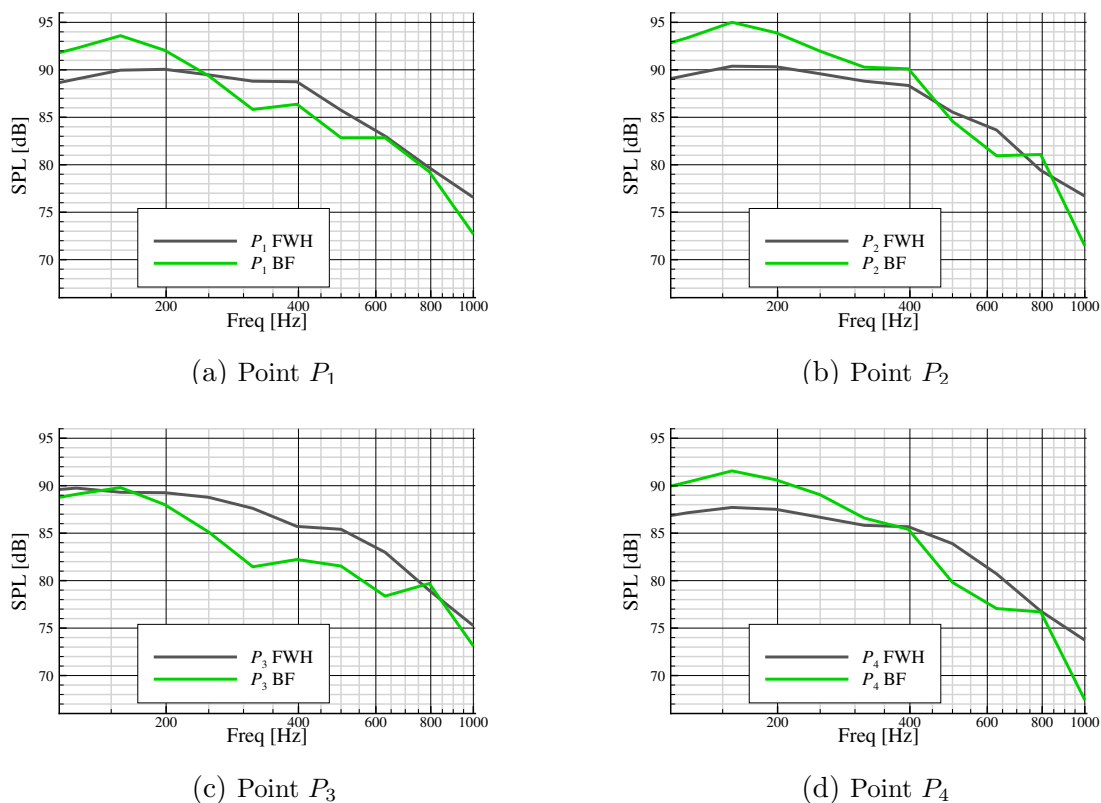


Figure 15. SPL spectra at mid-field points obtained by FWH and numerical beamforming (BF) methods. Dipole-type source with moment oriented along normals to the surface

Conclusions

This paper presents a numerical study of the noise sources generated by the wing of SSBJ prototype in landing mode.

A distinctive feature of this study is a combination of two ways of predicting and analyzing noise sources. The first is based on direct postprocessing of turbulent flow around the SSBJ airframe obtained by resource-inventive scale-resolving CFD/CAA simulation. The second is based on solving the inverse problem of noise source reconstruction using the acoustic data accumulated during CFD/CAA simulation. For the second approach, we apply the numerical beamforming method which assumes the near-field acoustics to be governed by the wave equation with a distributed source term in the right-hand side. It is for the first time that the numerical beamforming is used to analyze acoustic sources of the full-scale aircraft geometry.

An important detail of the study is the verification of the numerical beamforming by comparison SPL spectra for signals at mid-field points obtained by the FWH method and by radiation of acoustic perturbations from the noise sources detected by the numerical beamforming method.

According to the results of numerical beamforming and the SPL distributions obtained on the FWH surface, the main acoustic sources generated by the SSBJ wing in landing mode are located near the leading and trailing edges. PSD analysis of the acoustic pressure pulsations recorded under these edges shows that the loss of vortex stability near the edges of the SSBJ wing leads to the local increases in noise intensity. The analysis of the noise radiation patterns calculated using the FWH method demonstrates that the far-field noise has dominating dipole-type component for the one-third octave bands with central frequencies lower (see [7]) or equal to 250 Hz and dominating monopole-type component for the one-third octave bands with central frequencies equal to 1 kHz or higher. For the rest one-third octave bands, the noise radiation pattern probably has a mixed structure formed by both monopole-type and dipole-type components.

Acknowledgements

The research is carried out using the equipment of the shared research facilities of HPC computing resources at Lomonosov Moscow State University with the additional use of the hybrid supercomputer K60 installed in the Supercomputer Centre of Collective Usage of KIAM RAS.

This paper is distributed under the terms of the Creative Commons Attribution-Non Commercial 3.0 License which permits non-commercial use, reproduction and distribution of the work without further permission provided the original work is properly cited.

References

1. Abalakin, I.V., Bakhvalov, P.A., Bobkov, V.G., *et al.*: NOISEtte CFD&CAA Supercomputer Code for Research and Applications. Supercomput. Front. Innov. 11(2), 78–101 (aug 2024). <https://doi.org/10.14529/jsfi240206>
2. Bakhvalov, P.A., Kozubskaya, T.K., Kornilina, E.D., *et al.*: Technology of predicting acoustic turbulence in the far-field flow. Math. Model. Comput. Simulations 4(3), 363–373 (may 2012). <https://doi.org/10.1134/S2070048212030039>

3. Bakhvalov, P.A., Surnachev, M.D.: Method of averaged element splittings for diffusion terms discretization in vertex-centered framework. *J. Comput. Phys.* 450, 110819 (feb 2022). <https://doi.org/10.1016/J.JCP.2021.110819>
4. Bakhvalov, P., Kozubskaya, T., Rodionov, P.: EBR schemes with curvilinear reconstructions for hybrid meshes. *Comput. Fluids* 239, 105352 (may 2022). <https://doi.org/10.1016/J.COMPFLUID.2022.105352>
5. Barad, M.F., Kocheemoolayil, J.G., Kiris, C.C.: Lattice Boltzmann and Navier-Stokes Cartesian CFD Approaches for Airframe Noise Predictions. In: 23rd AIAA Comput. Fluid Dyn. Conf. AIAA AVIATION Forum, American Institute of Aeronautics and Astronautics (jun 2017). <https://doi.org/10.2514/6.2017-4404>
6. Deck, S., Renard, N.: Towards an enhanced protection of attached boundary layers in hybrid RANS/LES methods. *J. Comput. Phys.* 400, 108970 (2020). <https://doi.org/10.1016/j.jcp.2019.108970>
7. Duben, A.P., Kozubskaya, T.K., Rodionov, P.V.: Wing Noise Simulation of Supersonic Business Jet in Landing Configuration. *Supercomput. Front. Innov.* 11(3), 74–92 (oct 2024). <https://doi.org/10.14529/jsfi240305>
8. Ferris, R., Sacks, M., Cerizza, D., *et al.*: Aeroacoustic Computations of a Generic Low Boom Concept in Landing Configuration: Part 1 – Aerodynamic Simulations. *AIAA Aviat. Aeronaut. Forum Expo. AIAA Aviat. Forum 2021* (2021). <https://doi.org/10.2514/6.2021-2195>
9. Ffowcs Williams, J.E., Hawkings, D.L.: Sound generation by turbulence and surfaces in arbitrary motion. *Philos. Trans. R. Soc. London. Ser. A, Math. Phys. Sci.* 264(1151), 321–342 (may 1969). <https://doi.org/10.1098/rsta.1969.0031>
10. Gorobets, A.V., Duben, A.P., Kozubskaya, T.K., Rodionov, P.V.: Approaches to the Numerical Simulation of the Acoustic Field Generated by a Multi-Element Aircraft Wing in High-Lift Configuration. *Math. Model. Comput. Simulations* 15(1), 92–108 (feb 2023). <https://doi.org/10.1134/S2070048223010088>
11. Gorobets, A., Bakhvalov, P.: Heterogeneous CPU+GPU parallelization for high-accuracy scale-resolving simulations of compressible turbulent flows on hybrid supercomputers. *Comput. Phys. Commun.* 271, 108231 (feb 2022). <https://doi.org/10.1016/J.CPC.2021.108231>
12. Guseva, E.K., Garbaruk, A.V., Strelets, M.K.: An automatic hybrid numerical scheme for global RANS-LES approaches. *J. Phys. Conf. Ser.* 929(1), 012099 (nov 2017). <https://doi.org/10.1088/1742-6596/929/1/012099>
13. Karakulev, A., Kozubskaya, T., Plaksin, G., Sofronov, I.: Ffowcs Williams–Hawkings analogy for near-field acoustic sources analysis. *International Journal of Aeroacoustics* 21(5-7), 457–475 (2022). <https://doi.org/10.1177/1475472X221107367>
14. Khorrami, M.R., Fares, E.: Simulation-based airframe noise prediction of a full-scale, full aircraft. 22nd AIAA/CEAS Aeroacoustics Conf. 2016 (2016). <https://doi.org/10.2514/6.2016-2706>

15. Khorrami, M.R., Shea, P.R., Winski, C.S., *et al.*: Aeroacoustic Computations of a Generic Low Boom Concept in Landing Configuration: Part 3 – Aerodynamic Validation and Noise Source Identification. AIAA Aviat. Aeronaut. Forum Expo. AIAA Aviat. Forum 2021 (2021). <https://doi.org/10.2514/6.2021-2197>
16. Kozubskaya, T., Plaksin, G., Sofronov, I.: Statement of the beamforming problem and a method of its solution for the localization of an acoustic source based on computational experiment data. *Comput. Math. Math. Phys.* 61, 1864–1885 (11 2021). <https://doi.org/10.1134/S0965542521110129>
17. Kozubskaya, T., Plaksin, G., Sofronov, I.: On numerical beamforming for correlated dipole-type sources. *Computational Mathematics and Mathematical Physics* 63, 2162–2175 (12 2023). <https://doi.org/10.1134/S0965542523110131>
18. Liu, Y., Quayle, A., Dowling, A., Sijtsma, P.: Beamforming correction for dipole measurement using two-dimensional microphone arrays. *The Journal of the Acoustical Society of America* 124, 182–191 (07 2008). <https://doi.org/10.1121/1.2931950>
19. Mockett, C., Fuchs, M., Garbaruk, A., *et al.*: Two Non-zonal Approaches to Accelerate RANS to LES Transition of Free Shear Layers in DES. In: *Prog. Hybrid RANS-LES Model.*, vol. 130, pp. 187–201. Springer Verlag (2015). https://doi.org/10.1007/978-3-319-15141-0_15
20. Nicoud, F., Toda, H.B., Cabrit, O., *et al.*: Using singular values to build a subgrid-scale model for large eddy simulations. *Phys. Fluids* 23(8), 085106 (aug 2011). <https://doi.org/10.1063/1.3623274>
21. Plaksin, G.M., Kozubskaya, T.K., Sofronov, I.L.: On numerical beamforming for acoustic source identification basing on supercomputer simulation data. *Dokl. Math.* 110, 435–441 (2024). <https://doi.org/10.1134/S1064562424601550>
22. Ribeiro, A.F., Ferris, R., Khorrami, M.R.: Aeroacoustic Computations of a Generic Low Boom Concept in Landing Configuration: Part 2 – Airframe Noise Simulations. AIAA Aviat. Aeronaut. Forum Expo. AIAA Aviat. Forum 2021 (2021). <https://doi.org/10.2514/6.2021-2196>
23. Shur, M.L., Spalart, P.R., Strelets, M.K.: Noise Prediction for Increasingly Complex Jets. Part I: Methods and Tests. *Int. J. Aeroacoustics* 4(3), 213–245 (jul 2005). <https://doi.org/10.1260/1475472054771376>
24. Shur, M.L., Spalart, P.R., Strelets, M.K.: Noise Prediction for Increasingly Complex Jets. Part II: Applications. *Int. J. Aeroacoustics* 4(3), 247–266 (jul 2005). <https://doi.org/10.1260/72054771385>
25. Shur, M.L., Spalart, P.R., Strelets, M.K., Travin, A.K.: An Enhanced Version of DES with Rapid Transition from RANS to LES in Separated Flows. *Flow, Turbul. Combust.* 95(4), 709–737 (jun 2015). <https://doi.org/10.1007/S10494-015-9618-0>
26. Sijtsma, P.: Acoustic beamforming for the ranking of aircraft noise. Tech. rep., National Aerospace Laboratory NLR (2012), <https://api.semanticscholar.org/CorpusID:60149502>

27. Spalart, P.R., Allmaras, S.R.: A one-equation turbulence model for aerodynamic flows. In: AIAA Pap. 92-0439 (1992). <https://doi.org/10.2514/6.1992-439>
28. Voevodin, V.V., Antonov, A.S., Nikitenko, D.A., *et al.*: Supercomputer Lomonosov-2: Large Scale, Deep Monitoring and Fine Analytics for the User Community. Supercomput. Front. Innov. 6(2), 4–11 (jun 2019). <https://doi.org/10.14529/jsfi190201>
29. van der Vorst, H.A.: Bi-CGSTAB: A Fast and Smoothly Converging Variant of Bi-CG for the Solution of Nonsymmetric Linear Systems. SIAM J. Sci. Stat. Comput. 13(2), 631–644 (1992). <https://doi.org/10.1137/0913035>
30. Zaytsev, M.Y., Kopiev, V.F., Velichko, S.A., Belyaev, I.V.: Localization and ranking of aircraft noise sources in flight tests and comparison with acoustic measurements of a large-scale wing model. Acoust. Phys. 69(2), 182–192 (2023). <https://doi.org/10.1134/S1063771023700562>